

RESEARCH ARTICLE

# Supersonic gas jet stabilization in laser–plasma acceleration

Zhen-Zhe Lei<sup>1,3</sup>, Yan-Jun Gu<sup>1,3</sup>, Zhan Jin<sup>1,3</sup>, Shingo Sato<sup>1,3</sup>, Alexei Zhidkov<sup>1,3</sup>, Alexandre Rondepierre<sup>1,3</sup>, Kai Huang<sup>2,3</sup>, Nobuhiko Nakanii<sup>2,3</sup>, Izuru Daito<sup>2,3</sup>, Masakai Kando<sup>1,2,3</sup>, and Tomonao Hosokai<sup>1,3</sup>

<sup>1</sup>SANKEN (Institute of Scientific and Industrial Research), Osaka University, Ibaraki, Osaka, Japan

<sup>2</sup>Kansai Institute for Photon Science (KPSI), National Institutes for Quantum Science and Technology (QST), Kizugawa-city, Kyoto, Japan

<sup>3</sup>RIKEN SPring-8 Center, Sayo, Hyogo, Japan

(Received 20 September 2023; revised 11 October 2023; accepted 23 October 2023)

## Abstract

Supersonic gas jets generated via a conical nozzle are widely applied in the laser wakefield acceleration of electrons. The stability of the gas jet is critical to the electron injection and the reproducibility of the wakefield acceleration. Here we discussed the role of the stilling chamber in a modified converging–diverging nozzle to dissipate the turbulence and to stabilize the gas jets. By the fluid dynamics simulations and the Mach–Zehnder interferometer measurements, the instability originating from the nonlinear turbulence is studied and the mechanism to suppress the instability is proposed. Both the numerical and experimental results prove that the carefully designed nozzle with a stilling chamber is able to reduce the perturbation by more than 10% compared with a simple-conical nozzle.

**Keywords:** shock injection; hydrodynamic stability; laser wakefield acceleration; laser–plasma interaction

## 1. Introduction

Laser wakefield acceleration (LWFA) is attractive and promising to provide sources of radiation. It is expected to be a more compact facility compared with conventional accelerators<sup>[1,2]</sup>. A short pulse laser with ultra-high intensity ( $I > 10^{18}$  W/cm<sup>2</sup>) drives the plasma wave by expelling the electrons with its ponderomotive force. Background electrons in the plasma can be trapped and accelerated by the longitudinal electric fields of the waves to high energies over short distances. LWFA has experienced rapid development in the past decades and various mechanisms have been proposed for injection control, laser guidance and beam quality improvement<sup>[3–21]</sup>. Milestone achievements, including monoenergetic electron production and X-ray source beam generation, have been demonstrated in experiments<sup>[22–31]</sup>. State-of-the-art laser–plasma accelerators can already address the peak electron energy of approximately 7.8 GeV with the beam charge of tens of picocoulombs<sup>[32,33]</sup>. The energy spread of the electron

beam can be well controlled within several percent, while the lowest record is less than 1%<sup>[34,35]</sup>. All of these boost the development of laser wakefield accelerators as a novel branch of the accelerator family.

Apart from delivering more accessible high-energy electron beams, LWFA is expected to have potential applications in tomography and bright X-ray sources in material sciences, as well as in radiation therapy and pharmacology. However, the stability of LWFA is still far away from that required for applications. Similar to vacuum accelerators, LWFA devices consist of the common injection and acceleration parts that can constitute a staging system. The injection and acceleration processes in plasma are essentially nonlinear. Both processes, driven by a laser pulse, depend nonlinearly on its characteristics as well as on the characteristics of the target plasma. Therefore, the investigation of the entire acceleration process is extremely complicated. Usually investigations of the injection and acceleration processes are focused on optimizing the final parameters of the electron bunches, such as the peak energy, beam charge, emittance and energy spread. For that purpose, the laser pulse parameters, such as the pulse intensity, duration and waist, as well as the gas target parameters, such as the gas density, density profiles and gas compounds, are carefully

Correspondence to: Yan-Jun Gu, SANKEN (Institute of Scientific and Industrial Research), Osaka University, 8-1 Mihogaoka, Ibaraki, Osaka 567-0047, Japan. Email: [gu\\_yanjun@sanken.osaka-u.ac.jp](mailto:gu_yanjun@sanken.osaka-u.ac.jp)

chosen to provide the required characteristics of electron beams.

However, optimizing the laser and target parameters cannot thoroughly solve the problem of stability and reproducibility in the LWFA process. Even with the fixed parameters one observes essential fluctuations by a factor of 2–3 of electron bunch energy, bunch charges, energy spreads and beam emittances. Moreover, the poor pointing stability of bunches sometimes transfers to beam decomposition. It is apparent that the study of the sources for such instabilities differs from that of parameter optimization.

Owing to the nonlinearity of the injection and acceleration processes, there are many parameters resulting in the plasma dynamics. Therefore, the best way of seeking the sources of instabilities is to extract the phenomena responsible for different stages, such as the formation of targets, laser pulse focusing and propagation, electron self-injection and acceleration. Target formation is the first stage of LWFA. To maintain the reproducibility of the accelerated electron beam, it requires a stable gas target in the vacuum chamber with a precise density distribution profile. It guarantees that the laser and plasma interact in a proper density region ( $10^{18} - 10^{19} \text{ cm}^{-3}$ ) and the relative laser focal position does not shift too much from shot to shot. Usually, the stability and reproducibility of gas jets being formed for plasma are naturally assumed. However, shock waves and acoustic waves propagating in the gas flow may become the critical sources of instabilities. Thorough examination of the dynamics of the gas target is necessary to confirm and to exclude the possible sources of instability in LWFA.

In this paper, we numerically and experimentally studied the instability originating from the gas jet due to the nonlinear fluid dynamics in the supersonic nozzle. In LWFA, supersonic nozzles are commonly used to provide spatially well-defined supersonic gas targets with a plateau density profile and sharp gas-vacuum boundaries. The design and application of supersonic nozzles have been proposed in many theoretical and experimental works<sup>[36–42]</sup>. Costa *et al.*<sup>[43]</sup> studied the behaviour of the gas outflow with the variations of nozzle throat narrowing via both simulations and experiments. Their results point out that having a supersonic gas flow out of the nozzle is a better way to be able to influence the flow density. Furthermore, the smoothing angle of the nozzle throat has an influence on the output flow density value.

## 2. Theories and simulations

When the high-velocity flow shear is combined with a confining nozzle wall, the corresponding velocities significantly decrease due to the boundary effect. Such boundary effect is not only a singularity of the flow field providing the seed of the vortex and turbulence, but also partially blocks the cross-section of the nozzle, resulting in significant variations of gas pressure. Therefore, the gas target becomes unstable and the laser focal position may exceed the allowable misalignment. According to fluid dynamics simulations, the density uncertainty perturbation in a simple-conical nozzle reaches more than 10% and the longitudinal electron density profile shift is of the magnitude of submillimetres. However, if a stilling chamber is employed between the reservoir and the nozzle throat, the growth of the fluid instabilities can be effectively suppressed. The turbulences dissipate along the propagation in the stilling chamber. It results in a density profile uncertainty perturbation of less than 3% at the nozzle exit and the corresponding longitudinal shift is of the magnitude of micrometres. In this case, a more stable gas target prepared for laser irradiating can be expected. Here, the numerical calculations are proved by the experimental measurements via the Mach–Zehnder interferometric method<sup>[44–46]</sup>.

The fluid dynamics simulations are launched with ANSYS Fluent code, in which the Navier–Stokes equations are solved based on the finite volume method. To describe the turbulence, a shear-stress transport (SST)  $k-\omega$  model<sup>[47]</sup>, including the transport equations of the turbulence kinetic energy ( $k$ -equation) and the specific rate of dissipation ( $\omega$ -equation), is solved in addition to the conservation equations. Blending functions are applied to transit from the  $k-\omega$  model in the near-wall region to the free-stream independence of the  $k-\epsilon$  model in the far-field region.

A simple-conical nozzle is first examined here. The corresponding design and the numerical sketch are presented in Figures 1(a) and 1(b), respectively. The connection tube has a diameter of  $\phi_a = 1.5 \text{ mm}$ , the same as the nozzle throat. Above the throat, there is an expansion region for the gas flow until the nozzle exit, which has a diameter of  $\phi_b = 3 \text{ mm}$ . The lengths of the connection tube and the expansion region are  $L_a = 6 \text{ mm}$  and  $L_b = 8 \text{ mm}$ , respectively. To calculate the density distributions above the nozzle exit, a free fluid domain is employed in the numerical model with the outlet boundary condition on the top of the nozzle

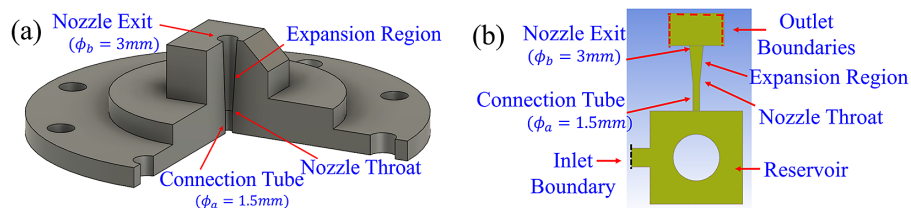


**Figure 1.** (a) Sketch of the simple-conical nozzle. (b) Schematic of the fluid dynamics simulation domains for the simple-conical nozzle.

(shown by the red dashed line in Figure 1(b)). The bottom domain in the numerical model represents the reservoir tank of the gas, which is not included in the corresponding sketch in Figure 1(a).

The complicated mechanical structure of the solenoid valve is simplified by a circular obstacle inside the tank in the fluid dynamics simulations. In experiments, a high-speed solenoid valve from SMARTSHELL Co., Ltd. (Ref. A2-6443-FL-403713) is employed. It has a gas inlet with 4 mm diameter and a gas exit with 1.5 mm diameter, which is equal to the nozzle throat. The gas is initially blocked by a conical stopping plug when the solenoid is not in operation. Once it is triggered, the plug can be detached 5 mm away from the gas exit, leaving enough space for the gas to be pumped without being choked. The solenoid valve is designed for pulsed control and the stopping plug reaches the maximum displacement within 100  $\mu$ s after being triggered. The fast motion guarantees a clean environment inside the chamber and relatively steady gas flow due to the fast gas loading. The opening state can be adjusted from 1.8 to 10 ms. In experiment, the opening time is set to be minimum, which is sufficient for gas loading. The closing action can be accomplished within 2 ms. The fluid dynamics simulation parameters are consistent with the experimental solenoid valve with a similar time scale for the steady flow formation.

The gas is pumped into the nozzle from the left-hand inlet (indicated by the black dashed line in Figure 1(b)) with the pressure input boundary condition, which is equivalent to that connected with a constant pressure reservoir. The initial pumping pressure is set to be a constant at  $p_0 = 0.6$  MPa in all the fluid dynamics simulation cases, which corresponds to a jet duration of 2 ms. According to the 1D isentropic flow model<sup>[48]</sup>, the evolution of the Mach number, density and pressure of the gas along the nozzle can be predicted as follows:

$$\frac{A^*}{A} = M \left[ 1 + \frac{\gamma-1}{\gamma+1} (M^2 - 1) \right]^{-\frac{\gamma+1}{2(\gamma-1)}}, \quad (1)$$

$$\frac{\rho}{\rho_0} = \left( 1 + \frac{\gamma-1}{2} M^2 \right)^{-\frac{1}{\gamma-1}}, \quad (2)$$

$$\frac{T}{T_0} = \left( 1 + \frac{\gamma-1}{2} M^2 \right)^{-1}, \quad (3)$$

$$\frac{p}{p_0} = \left( 1 + \frac{\gamma-1}{2} M^2 \right)^{-\frac{\gamma}{\gamma-1}}, \quad (4)$$

where  $A^*$  represents the cross-section at the nozzle throat and  $\rho_0$ ,  $T_0$  and  $p_0$  are the initial density, temperature and pressure for the gas, respectively. In all the simulations, the initial gas flow is selected to be ideal hydrogen at room temperature,  $T_0 = 300$  K. Therefore, the specific heat ratio of the gas is

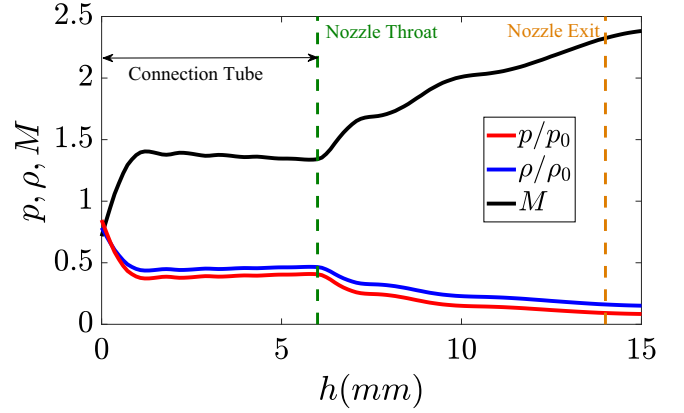


**Figure 2.** (a) Profiles of gas density, pressure and Mach number along the vertical direction from the connection tube to the exit. The density and pressure are normalized to the initial condition.

$\gamma = 1.41$ . The grid resolution varies from 20 to 100  $\mu$ m according to the characteristic size of the specified domain. The total amount of the grid is typically of the magnitude of  $10^6$ .

For an ideal isentropic nozzle with the exit size double that of the throat, the hydrogen flow becomes supersonic with the Mach number of  $M = 2.9$  based on Equation (1). The gas density and pressure decrease after the nozzle throat. In the simple-conical nozzle case, the isentropic condition is not fully satisfied. The gas flow expansion is non-adiabatic with the frictional and dissipative losses. Therefore, the Mach number at the exit is about  $M = 2.4$ , as seen in Figure 2, which is slightly lower than the ideal isentropic prediction. In principle, with the gas jet having the obtained Mach number

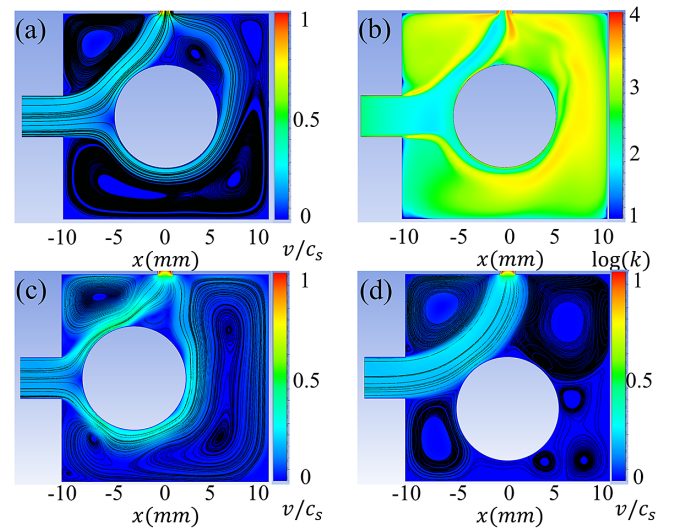


**Figure 3.** (a) Velocity distribution (normalized to the sound speed) and streamlines in the gas reservoir part. (b) Distribution of the turbulent kinetic energy in the gas reservoir part with a logarithmic scale. (c), (d) Velocity distributions and streamlines for the cases of left and down shift in the reservoir, respectively.

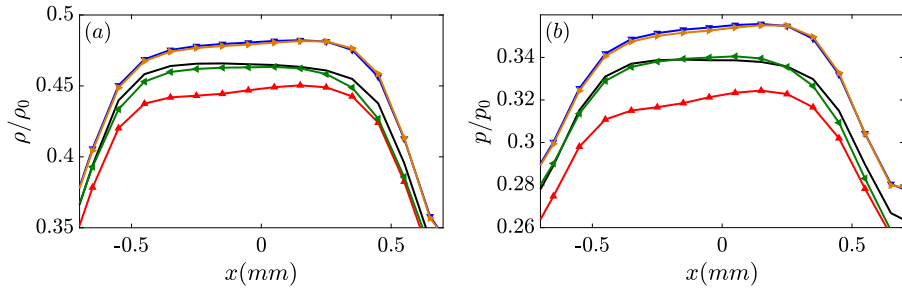


**Figure 4.** (a) Gas density and (b) pressure profiles at the nozzle throat obtained in the different initial shift cases (black-none, red-up, blue-down, green-left, orange-right), respectively. The triangle marker directions refer to the shift directions of the central obstacle.

and the density shown in Figure 2, it is possible to have laser-plasma interaction, such as wakefield acceleration, with shock injections. However, the stability of the gas jet from the simple-conical nozzle is rather poor. It is necessary to understand the potential mechanism of such instability and then to suppress or dissipate it.

To generate the supersonic jet, the hydrogen gas is first pumped into the reservoir and then injected into the nozzle with the control of the solenoid valve. Due to the complicated structure of the reservoir and the valve motion, it is difficult to control the flow state from shot to shot during the pulse pumping. Figure 3(a) shows the velocity distribution of the gas flow with the streamlines (in black) in the reservoir. Vortex structures and eddies are clearly formed due to the interaction of the high-velocity flow and the static wall. Between the boundary walls and the central obstacle, there is a narrow steady flow with relatively high velocity. From the streamlines, one finds that the eddy regions have low flow velocities referring to local stagnation, which changes the pressure and the density distributions. The turbulent kinetic energy measured by the root mean square of the fluctuation in the flow velocity,  $k = \Sigma(u_i - \bar{u}_i)^2/2$ , in the corresponding region is presented in Figure 3(b). The intensity of turbulence around the eddies is two orders of magnitude higher than that of the steady flow part. The eddies and strong turbulent kinetic energy make the accurate prediction of the flow quite challenging, that is, the gas jet generated from the nozzle becomes unstable and unreproducible.

An initial perturbation is introduced into the fluid dynamics simulations to describe the stochastics of the valve motion. A group of simulations is launched by slightly shifting the central obstacle in the reservoir by 2 mm in the up, down, left and right directions, respectively. All of the other conditions are identical in these simulations. Two typical cases corresponding to the left-hand side and down-side shift are presented in Figures 3(c) and 3(d). The vortex distributions and the flow paths are significantly changed in these cases, as seen in Figures 3(a), 3(c) and 3(d). As a result, the gas flows being pumped into the nozzle are actually not identical under different conditions. In Figures 4(a) and 4(b), the gas density and pressure under different conditions are

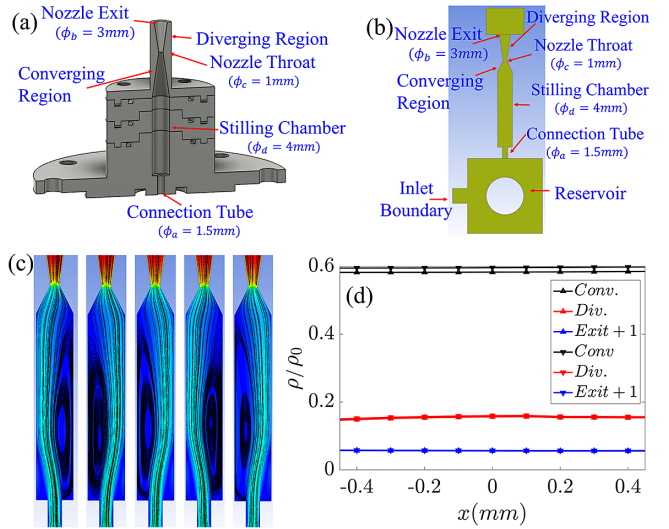


**Figure 5.** (a) Sketch of the converging–diverging nozzle. (b) Schematic of the fluid dynamics simulation domains for the converging–diverging nozzle. (c) Velocity distributions (normalized to the sound speed) and streamlines inside the stilling chamber part. The subplots from left to right correspond to the non-, up-, down-, left- and right-shift cases, respectively. (d) The density profiles in the converging region, diverging region and 1 mm above the exit are compared between the up-shift and down-shift cases.

compared. The profiles are taken along the cross-section of the nozzle throat averaged within 0.5 mm in the vertical direction. The density perturbations reach 10%, while the density peak position shifts about 1 mm. For laser–plasma experiments, such as shock injections, the acceleration effect relies on the stability of the shock formation and the density downramp profile, which is very sensitive to the outflow angle and the Mach number of the gas jet.

In order to stabilize the gas flow, a stilling chamber with a length of 20 mm and a diameter of  $\phi_d = 4$  mm is added above the connection tube. A converging–diverging shape is employed, as seen in Figures 5(a) and 5(b). The converging and diverging parts have the lengths of 10.5 and 8.5 mm, respectively. The nozzle throat has a diameter of  $\phi_c = 1$  mm and the exit diameter is  $\phi_b = 3$  mm. Here, the nozzle throat is set to be smaller than that of the solenoid valve exit. The reservoir and inlet boundaries are identical to the previous simple-conical nozzle case. To connect the reservoir with the stilling chamber, a tube with  $\phi_a = 1.5$  mm diameter and 3 mm

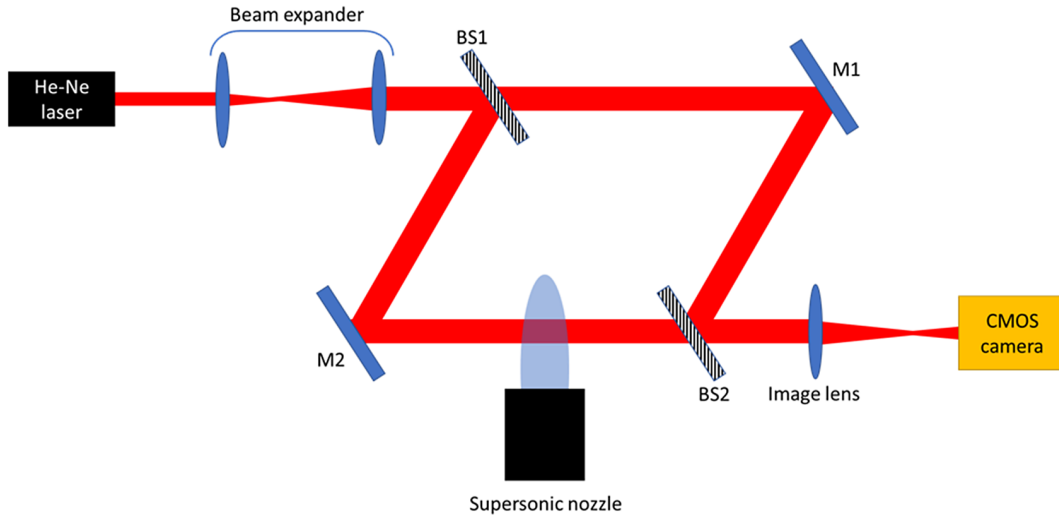


**Figure 6.** Experimental schematic diagram of the Mach–Zehnder interferometer setup.

height is employed. Similar to the operations applied in the simple-conical nozzle case, the central obstacle here is also shifted to introduce similar initial perturbations. Figure 5(c) presents the velocity distributions and streamlines inside the stilling chamber for all shift cases. The different vortex and the eddy structures originate from the uncertainty in the reservoirs, as discussed in the simple-conical case. The incoming gas flows keep the velocity components disturbed by the vortex in the reservoir, resulting in different bending directions in the chamber. However, the turbulent structures show a clear dissipative tendency along the chamber. Once the gas flow enters the converging region, the fluids become similar in all cases. To prove this, the density profiles in the converging, diverging and exit regions are compared between the up-shift and down-shift cases (shown in Figure 5(d)). The density discrepancy in the converging region is about 2.4%, which is already significantly smaller than that of the previous simple-conical nozzle case. In the region of 1 mm above the exit (blue lines), that is, the common laser–plasma interaction region, the corresponding discrepancy further drops to 1.8%. Therefore, the gas jet prepared by a converging–diverging nozzle with a stilling chamber becomes much more stable to reproduce similar density profiles from shot to shot.

### 3. Experimental results

The stabilization effect of the converging–diverging nozzle is also confirmed by the experimental measurement. We characterize our supersonic nozzles with a Mach–Zehnder interferometer method, as seen in Figure 6. A continuous-wave (CW) He-Ne laser ( $\lambda = 633$  nm) was used as a probe beam. To obtain the complete picture of the gas jet, a beam expander was installed in the laser beam line. The beam size after the beam expander was 20 mm in diameter. The expanded laser beam was split and rejoined

**Table 1.** S-C nozzle and C-D nozzle represent the simple-conical nozzle and the converging–diverging nozzle, respectively. (Values not in bold are taken from the fluid dynamics simulations, while those in bold are obtained from the experimental measurements. Std. represents the standard deviation from 20 shots in the experiment and five cases in simulations. Max. represents the maximum discrepancy in the 20 shots in the experiment and five cases in simulations.)

	S-C nozzle	C-D nozzle
Std. (%)	4.7/ <b>4.5</b>	<b>1/1.3</b>
Max. (%)	13.5/ <b>13</b>	<b>2.5/3</b>

by using two beam splitters (BS1 and BS2, Thorlabs). The gas jet image was generated by an  $f/12.5$  image lens ( $f = 750$  mm) and picked up by a complementary metal-oxide-semiconductor (CMOS) camera (The Imaging Source, DMK33GX174e). The camera exposure time was set to the minimum, which equals 30  $\mu$ s. Since the reflective index of the gas target is different from air, this causes the interference fringes to bend in the gas jet region. From the phase change of the interferometry patterns, the gas density of the nozzle can be calculated. For safety concerns, we use nitrogen for the target gas since nitrogen and hydrogen have similar  $\gamma$  values at room temperature. From the previous simulations, we noticed that changing the reservoir tank pressure from 0.6 to 3 MPa would not affect the supersonic gas jet shape. Only the absolute density value will be changed. To get enough phase shift on the interferometry pattern, we set the tank pressure to 3 MPa since the phase shift is related to the gas density. To compare the stability of those two gas jets as the plasma targets for LWFA, 20 consecutive shots at 2 mm above the nozzle are measured. To obtain the gas density distribution, the Abel inversion is operated to generate the phase map. The experimental results for the gas density perturbation are summarized in Table 1, together with the simulation results. Values not in

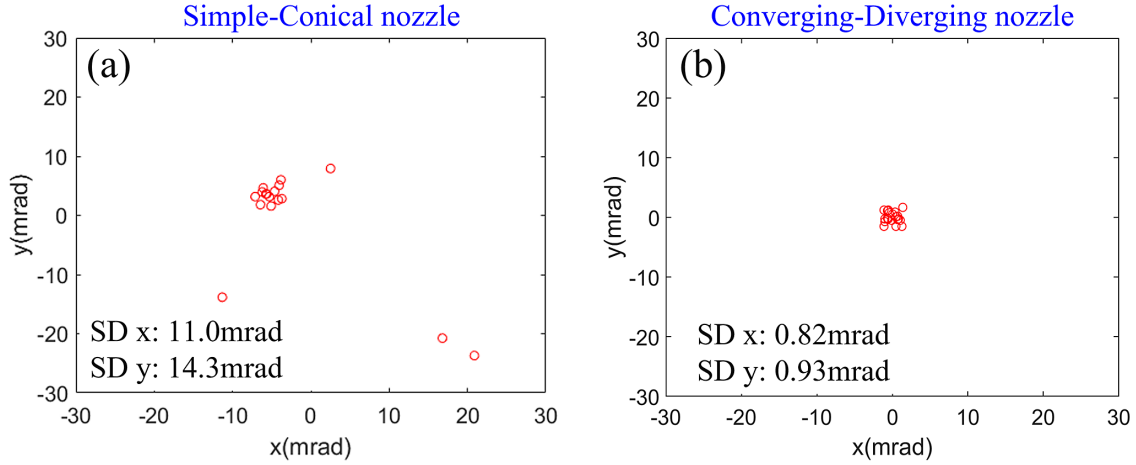


**Figure 7.** Electron beam pointing distributions obtained in experiments with (a) the simple-conical nozzle and (b) the converging–diverging nozzle.

bold are taken from fluid dynamics simulations, while those in bold are obtained from the experimental measurements. Std. represents the standard deviation from 20 shots in the experiment and five cases in the simulations. Max. represents the maximum discrepancy ratio. The statistical results from the experimental measurements are well consistent with the simulations. Both of them show that the density uncertainty in the converging–diverging nozzle is much lower.

To further confirm the stabilizing effect by adding the stilling chamber, the simple-conical nozzle and the converging–diverging nozzle are both tested in the LWFA experiments with the shock injection scheme<sup>[5,6]</sup>, which were carried out with the Laser Acceleration Platform (LAPLACIAN) Ti:sapphire laser system (Amplitude Technologies) at RIKEN SPring-8 Center based on a chirped pulse amplification (CPA) technique. An ultra-short laser pulse ( $\tau = 24$  fs) with a peak power of 50 TW is delivered. Details of the experimental setup can be found in Ref. [49]. The electron bunch obtained with this proposed supersonic gas jet has a typical length of about 3  $\mu\text{m}$ . The electron pointing stability results obtained within 20 shots for each type of nozzle are presented in Figure 7. The 20 shots with the converging–diverging nozzle are concentrated, while the 20 shots with the simple-conical nozzle have a more than 10 times larger standard deviation in both the  $x$ - and  $y$ -directions. Since the irradiating laser conditions are identical in both cases, the pointing fluctuations from the laser system are excluded here. Therefore, one can draw the conclusion that the improvement of the electron pointing stability is contributed by the nozzle design, that is, the dissipation process in the stilling chamber.

#### 4. Conclusions

In summary, a method for generating stable and reproducible supersonic gas jets for laser–plasma interaction is proposed. The stilling chamber in a modified converging–diverging

nozzle plays an important role in dissipating the nonlinear instabilities originated from the fluid boundary effects and the uncertainties of the solenoid valve pumping. Both the fluid dynamics simulations and the experimental measurements confirm that the density profiles of the converging–diverging nozzle have much lower perturbations than that of a simple-conical nozzle. In the LWFA experiments with a shock injection mechanism, the high electron pointing stability is obtained in the converging–diverging nozzle case. As such, the study proves the validity of the stilling chamber in stabilizing the gas jet, which will be useful and important to potential laser–plasma applications.

#### Acknowledgements

This work was funded by the JST-MIRAI program, grant No. JPMJMI17A1. We are grateful to the technical teams of the SPring-8 Center for their support of the Laser Acceleration Platform. We acknowledge the use of the supercomputer facility of the Cybermedia Centre at Osaka University. We also thank SMARTSHELL Co., Ltd for technical support on high-speed solenoid valves and related systems.

#### References

1. T. Tajima and J. M. Dawson, *Phys. Rev. Lett.* **43**, 267 (1979).
2. E. Esarey, C. B. Schroeder, and W. P. Leemans, *Rev. Mod. Phys.* **81**, 1229 (2009).
3. D. Umstadter, J. K. Kim, and E. Dodd, *Phys. Rev. Lett.* **76**, 2073 (1996).
4. T. Hosokai, M. Kando, H. Dewa, H. Kotaki, S. Kondo, N. Hasegawa, K. Nakajima, and K. Horioka, *Opt. Lett.* **25**, 10 (2000).
5. P. Tomassini, M. Galimberti, A. Giulietti, D. Giulietti, L. A. Gizzi, L. Labate, and F. Pegoraro, *Phys. Rev. Spec. Top. Accel. Beams* **6**, 121301 (2003).
6. H. Suk, N. Barov, J. B. Rosenzweig, and E. Esarey, *Phys. Rev. Lett.* **86**, 1011 (2001).
7. J. Faure, C. Rechatin, A. Norlin, A. Lifschitz, Y. Glinec, and V. Malka, *Nature* **444**, 737 (2006).

8. W. P. Leemans, B. Nagler, A. J. Gonsalves, C. Tóth, K. Nakamura, C. G. R. Geddes, E. Esarey, C. B. Schroeder, and S. M. Hooker, *Nat. Phys.* **2**, 696 (2006).
9. T. Hosokai, K. Kinoshita, A. Zhidkov, A. Maekawa, A. Yamazaki, and M. Uesaka, *Phys. Rev. Lett.* **97**, 075004 (2006).
10. X. Davoine, E. Lefebvre, C. Rechatin, J. Faure, and V. Malka, *Phys. Rev. Lett.* **102**, 065001 (2009).
11. M. Chen, E. Esareya, C. B. Schroeder, C. G. R. Geddes, and W. P. Leemans, *Phys. Plasmas* **19**, 033101 (2012).
12. R. Lehe, A. F. Lifschitz, X. Davoine, C. Thauray, and V. Malka, *Phys. Rev. Lett.* **111**, 085005 (2013).
13. S. Corde, C. Thauray, A. Lifschitz, G. Lambert, K. T. Phuoc, X. Davoine, R. Lehe, D. Douillet, A. Rousse, and V. Malka, *Nat. Commun.* **4**, 1501 (2013).
14. A. Buck, J. Wenz, J. Xu, K. Khrennikov, K. Schmid, M. Heigoldt, J. M. Mikhailova, M. Geissler, B. Shen, F. Krausz, S. Karsch, and L. Veisz, *Phys. Rev. Lett.* **110**, 185006 (2013).
15. F. Li, J. F. Hua, X. L. Xu, C. J. Zhang, L. X. Yan, Y. C. Du, W. H. Huang, H. B. Chen, C. X. Tang, W. Lu, C. Joshi, W. B. Mori, and Y. Q. Gu, *Phys. Rev. Lett.* **111**, 015003 (2013).
16. N. Bourgeois, J. Cowley, and S. M. Hooker, *Phys. Rev. Lett.* **111**, 155004 (2013).
17. M. Zeng, M. Chen, L. L. Yu, W. B. Mori, Z. M. Sheng, B. Hidding, D. A. Jaroszynski, and J. Zhang, *Phys. Rev. Lett.* **114**, 084801 (2015).
18. M. P. Tooley, B. Ersfeld, S. R. Yoffe, A. Noble, E. Brunetti, Z. M. Sheng, M. R. Islam, and D. A. Jaroszynski, *Phys. Rev. Lett.* **119**, 044801 (2017).
19. Z. Jin, H. Nakamura, N. Pathak, Y. Sakai, A. Zhidkov, K. Sueda, R. Kodama, and T. Hosokai, *Sci. Rep.* **9**, 20045 (2019).
20. D. N. Gupta, S. R. Yoffe, A. Jain, B. Ersfeld, and D. A. Jaroszynski, *Sci. Rep.* **12**, 20368 (2022).
21. K. V. Grafenstein, F. M. Foerster, F. Haberstroh, D. Campbell, F. Irshad, F. C. Salgado, G. Schilling, E. Travac, N. Weiße, M. Zepf, A. Döpp, and S. Karsch, *Sci. Rep.* **13**, 11680 (2023).
22. J. Faure, Y. Glinec, A. Pukhov, S. Kiselev, S. Gordienko, E. Lefebvre, J. P. Rousseau, F. Burgy, and V. Malka, *Nature* **431**, 541 (2004).
23. S. P. D. Mangles, C. D. Murphy, Z. Najmudin, A. G. R. Thomas, J. L. Collier, A. E. Dangor, E. J. Divall, P. S. Foster, J. G. Gallacher, C. J. Hooker, D. A. Jaroszynski, A. J. Langley, W. B. Mori, P. A. Norreys, F. S. Tsung, R. Viskup, B. R. Walton, and K. Krushelnick, *Nature* **431**, 535 (2004).
24. C. G. R. Geddes, C. Toth, J. van Tilborg, E. Esarey, C. B. Schroeder, D. Bruhwiler, C. Nieter, J. Cary, and W. P. Leemans, *Nature* **431**, 538 (2004).
25. I. Blumenfeld, C. E. Clayton, F. J. Decker, M. J. Hogan, C. K. Huang, R. Ischebeck, R. Iverson, C. Joshi, T. Katsouleas, N. Kirby, W. Lu, K. A. Marsh, W. B. Mori, P. Muggli, E. Oz, R. H. Siemann, D. Walz, and M. M. Zhou, *Nature* **445**, 741 (2007).
26. S. Kneip, C. McGuffey, J. L. Martins, S. F. Martins, C. Bellei, V. Chvykov, F. Dollar, R. Fonseca, C. Huntington, G. Kalintchenko, A. Maksimchuk, S. P. D. Mangles, T. Matsuo, S. R. Nagel, C. A. J. Palmer, J. Schreiber, K. T. Phuoc, A. G. R. Thomas, V. Yanovsky, L. O. Silva, K. Krushelnick, and Z. Najmudin, *Nat. Phys.* **6**, 980 (2010).
27. K. T. Phuoc, S. Corde, C. Thauray, V. Malka, A. Tafzi, J. P. Goddet, R. C. Shah, S. Sebban, and A. Rousse, *Nat. Photonics* **6**, 308 (2012).
28. N. D. Powers, I. Ghebregziabher, G. Golovin, C. Liu, S. Chen, S. Banerjee, J. Zhang, and D. P. Umstadter, *Nat. Photonics* **8**, 28 (2014).
29. M. Litos, E. Adli, W. An, C. I. Clarke, C. E. Clayton, S. Corde, J. P. Delahaye, R. J. England, A. S. Fisher, J. Frederico, S. Gessner, S. Z. Green, M. J. Hogan, C. Joshi, W. Lu, K. A. Marsh, W. B. Mori, P. Muggli, N. Vafaei-Najafabadi, D. Walz, G. White, Z. Wu, V. Yakimenko, and G. Yocky, *Nature* **515**, 92 (2014).
30. E. Adli, A. Ahuja, O. Apsimon, R. Apsimon, A.-M. Bachmann, D. Barrientos, F. Batsch, J. Bauche, V. K. Berglyd Olsen, M. Bernardini, T. Bohl, C. Bracco, F. Braumüller, G. Burt, B. Buttenschön, A. Caldwell, M. Cascella, J. Chappell, E. Chevallay, M. Chung, D. Cooke, H. Damerau, L. Deacon, L. H. Deubner, A. Dexter, S. Doebert, J. Farmer, V. N. Fedosseev, R. Fiorito, R. A. Fonseca, F. Friebel, L. Garolfi, S. Gessner, I. Gorgisyan, A. A. Gorn, E. Granados, O. Grulke, E. Gschwendtner, J. Hansen, A. Helm, J. R. Henderson, M. Hüther, M. Ibison, L. Jensen, S. Jolly, F. Keeble, S.-Y. Kim, F. Kraus, Y. Li, S. Liu, N. Lopes, K. V. Lotov, L. Maricalva Brun, M. Martyanov, S. Mazzoni, D. Medina Godoy, V. A. Minakov, J. Mitchell, J. C. Molendijk, J. T. Moody, M. Moreira, P. Muggli, E. Öz, C. Pasquino, A. Pardons, F. Peña Asmus, K. Pepitone, A. Perera, A. Petrenko, S. Pitman, A. Pukhov, S. Rey, K. Rieger, H. Ruhl, J. S. Schmidt, I. A. Shalimova, P. Sherwood, L. O. Silva, L. Soby, A. P. Sosedkin, R. Speroni, R. I. Spitsyn, P. V. Tuv, M. Turner, F. Velotti, L. Verra, V. A. Verzilov, J. Vieira, C. P. Welsch, B. Williamson, M. Wing, B. Woolley, and G. Xia, *Nature* **561**, 363 (2018).
31. W. T. Wang, K. Feng, L. Ke, C. Yu, Y. Xu, R. Qi, Y. Chen, Z. Qin, Z. Zhang, M. Fang, J. Liu, K. Jiang, H. Wang, C. Wang, X. Yang, F. Wu, Y. Leng, J.-S. Liu, R. Li, and Z. Xu, *Nature* **595**, 516 (2021).
32. W. P. Leemans, A. J. Gonsalves, H.-S. Mao, K. Nakamura, C. Benedetti, C. B. Schroeder, C. Tóth, J. Daniels, D. E. Mittelberger, S. S. Bulanov, J.-L. Vay, C. G. R. Geddes, and E. Esarey, *Phys. Rev. Lett.* **113**, 245002 (2014).
33. A. J. Gonsalves, K. Nakamura, J. Daniels, C. Benedetti, C. Pieronek, T. C. H. de Raadt, S. Steinke, J. H. Bin, S. S. Bulanov, J. van Tilborg, C. G. R. Geddes, C. B. Schroeder, C. Tóth, E. Esarey, K. Swanson, L. Fan-Chiang, G. Bagdasarov, N. Bobrova, V. Gasilov, G. Korn, P. Sasorov, and W. P. Leemans, *Phys. Rev. Lett.* **122**, 084801 (2019).
34. A. Döpp, C. Thauray, E. Guillaume, F. Massimo, A. Lifschitz, I. Andriyash, J. P. Goddet, A. Tafzi, K. T. Phuoc, and V. Malka, *Phys. Rev. Lett.* **121**, 074802 (2018).
35. L. T. Ke, K. Feng, W. T. Wang, Z. Y. Qin, C. H. Yu, Y. Wu, Y. Chen, R. Qi, Z. J. Zhang, Y. Xu, X. J. Yang, Y. X. Leng, J. S. Liu, R. X. Li, and Z. Z. Xu, *Phys. Rev. Lett.* **126**, 214801 (2021).
36. S. Semushin and V. Malka, *Rev. Sci. Instrum.* **72**, 2961 (2001).
37. K. Schmid and L. Veisz, *Rev. Sci. Instrum.* **83**, 053304 (2012).
38. S. Lorenz, G. Grittani, E. Chacon-Golcher, C. M. Lazzarini, J. Limpouch, F. Nawaz, M. Nevrkla, L. Vilanova, and T. Levato, *Matter Radiat. Extremes* **4**, 015401 (2019).
39. L. Rovige, J. Huijts, A. Vernier, I. Andriyash, F. Sylla, V. Tomkus, V. Girdauskas, G. Raciukaitis, J. Dudutis, V. Stankevici, P. Gecys, and J. Faure, *Rev. Sci. Instrum.* **92**, 083302 (2021).
40. C. Aniculaesei, H. T. Kim, B. J. Yoo, K. H. Oh, and C. H. Nam, *Rev. Sci. Instrum.* **89**, 025110 (2018).
41. H. Xu, G. Chen, D. Patel, Y. Cao, L. Ren, H. Xu, H. Shao, J. He, and D. E. Kim, *AIP Adv.* **11**, 075313 (2021).
42. O. Zhou, H.-E. Tsai, T. M. Ostermayr, L. Fan-Chiang, J. Tilborg, C. B. Schroeder, E. Esarey, and C. G. R. Geddes, *Phys. Plasmas* **28**, 093107 (2021).
43. G. Costa, M. P. Anania, A. Biagioni, F. G. Bisesto, M. Del Franco, M. Galletti, M. Ferrario, R. Pompili, S. Romeo, A. R. Rossi, A. Zigler, and A. Cianchi, *JINST* **17**, C01049 (2022).
44. F. Brandi and F. Giammanco, *Opt. Express* **19**, 25479 (2011).
45. J. Couperus, A. Köhler, T. A. W. Wolterink, A. Jochmann, O. Zarini, H. M. J. Bastiaens, K. J. Boller, A. Irman, and U.

- Schramm, Nucl. Instrum. Methods Phys. Res. Sect. A **830**, 504 (2016).
46. A. Adelman, B. Hermann, R. Ischebeck, M. C. Kaluza, U. Locans, N. Sauerwein, and R. Tarkeshian, Appl. Sci. **8**, 443 (2018).
47. F. R. Menter, AIAA J. **32**, 1598 (1994).
48. J. D. Anderson Jr., *Fundamentals of Aerodynamics* (McGraw Hill, New York, 2010).
49. Z. Lei, Z. Jin, A. Zhidkov, N. Pathak, Y. Mizuta, K. Huang, N. Nakanii, I. Daito, M. Kando, and T. Hosokai, Prog. Theor. Exp. Phys. **2023**, 033J01 (2023).